Nonlinear electron-phonon coupling in doped manganites
Supplementary Materials

V. Esposito,[1,*] M. Fechner,[2,3] R. Mankowsky,[2,4] H. Lemke,[5,6] M. Chollet,[5] J.M. Glownia,[5] M. Nakamura,[7] M. Kawasaki,[7,8] Y. Tokura,[7,8] U. Staub,[1] P. Beaud,[1,6] and M. Först[2,4]

[1]*Swiss Light Source, Paul Scherrer Institut, 5232 Villigen PSI, Switzerland*

[2]*Max-Planck Institute for the Structure and Dynamics of Matter, 22761 Hamburg, Germany*

[3]*Materials Theory, ETH Zürich, Wolfgang-Pauli-Strasse 27, 8093 Zürich, Switzerland*

[4]*Center for Free Electron Laser Science, 22761 Hamburg, Germany*

[5]*LCLS, SLAC National Accelerator Laboratory, Menlo Park, California 94025, USA*

[6]*SwissFEL, Paul Scherrer Institut, 5232 Villigen PSI, Switzerland*

[7]*RIKEN Center for Emergent Matter Science, Wako 351-0198, Japan*

[8]*Department of Applied Physics and Quantum Phase Electronics Center (QPEC), University of Tokyo, Tokyo 113-8656, Japan*

(Dated: May 12, 2017)

PUMP POLARIZATION AND CRYSTAL ORIENTATION

In order to excite a desired IR active phonon mode, the driving electric field has to point along a specific crystallographic direction. This is, however, not the only geometrical experimental constraint, as the crystal orientation in the laboratory frame is also defined by the diffraction condition for the reflection that is being probed. Because the pump polarization cannot be rotated (it is set horizontally in the laboratory frame) both criteria have to be fulfilled together. The only variable degrees of freedom left are then the incident angles of both beams. But other constraints are the time resolution which is optimized with collinear pump and probe beams and the diffracted intensity that is maximized at smaller grazing incidence angles. Although there is no general solution we can optimize the electric field of the pump light along a specific axis by carefully choosing the appropriate sample domain and incident angles. The pump polarization angle to the c-axis is given in Table S1 for two possible domains with a mid-IR incident angle of 45°, a grazing X-ray angle of 15° and at the $(0\bar{3}0)$ diffraction condition. This choice of incident angles only slightly increases the time resolution from 200 to 220 fs, while keeping a decent diffracted signal and the electric pump field polarized mainly along the desired c- or to the a-axis when looking at different domains in the film.

Domain	hkl	γ	α
$(\bar{1}\bar{1}2)$	$(0\bar{3}0)$	32°	61°
$(1\bar{1}2)$	$(0\bar{3}0)$	82°	21°

TABLE I. Pump polarization angle to the axis of the crystal. The domain is defined by its surface normal; the angle γ is the angle to the c-axis and α is the angle to the a-axis.

PUMP POLARIZATION DEPENDENCE OF THE PHOTO-INDUCED PHASE TRANSITION

While most of the experiment has been performed on the $(0\bar{3}0)$ peak of the $(\bar{1}\bar{1}2)$ domain, data were also taken on the $(1\bar{1}2)$ domain, where the electric field of the pump is polarized in the ab-plane (Fig. 1). We observe a complete melting of the charge order for both directions of excitation. The excitation along the c-axis is, however, slightly more efficient than in the

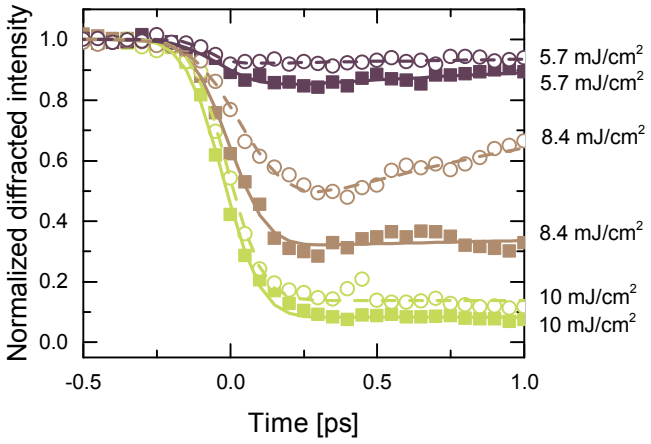

FIG. 1. Transient response of the $(0\bar{3}0)$ reflection upon excitation of orthogonal modes at 140 K. The full square symbols are for an excitation along the c-axis and the empty circles for an excitation in the ab-plane.

ab-plane, even more so when considering that the extinction coefficient (Fig. 1 (b)) along the a and b axes (3.2 m-1) is larger than along the c-axis (2.9 μm^{-}1).The difference in efficiency could be explained by a small difference in the coupling strength to the electronic degrees of freedom. This is interesting, as the charge and orbital order develop within the ab-plane and one might intuitively expect that atomic motion within this plane would couple more strongly to the underlying electronic order.

DFT AND CALCULATION OF THE PHONON MODE

The first principle calculations are performed in the framework of density functional theory using the generalized gradient approximation (GGA) [1] as implemented within the Vienna ab-initio simulation package (VASP) [2]. All our calculations are done with the default projector augmented wave (PAW) pseudopotentials [3] which exhibit the following electronic configurations: Pr ($6p^1$, $6s^2$, $5p^6$,$5s^2$), Ca ($3s^2$,$3p^6$), Mn ($3d^5$, $4s^2$, $3p^6$) and O ($2s^2$, $2p^4$). To take into account strong correlation effects, we employ a $DFT+U$ scheme [4] with $U = 5.0$ eV and $J = 0.0$ eV applied to the Mn d-states. We select these values to reproduce the experimental band gap of 0.37 eV [5]. After testing the convergence of forces, phonon frequencies and anharmonic coupling constants, we chose a 3x5x7 k-point mesh in

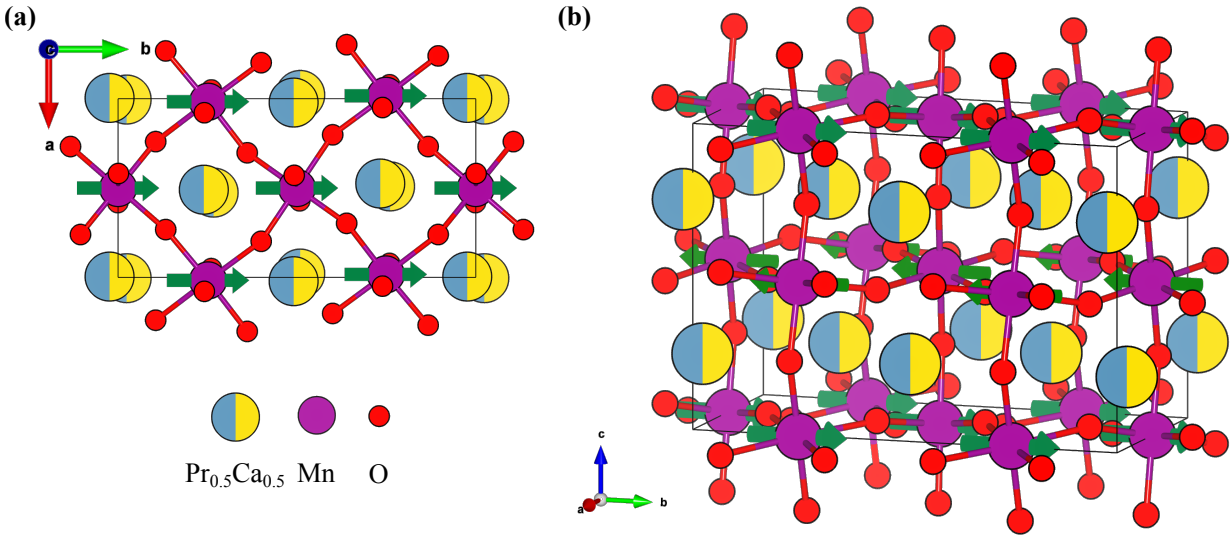

FIG. 2. Two different perspective on the PCMO unit cell. The green arrows on the Mn atoms represent the local spin arrangement for the A-type antiferromagnetic ordering.

combination with a cutoff energy for the plane wave basis set of 550 eV. We further perform structural relaxations, to obtain force free reference structures, required for computations of the phonon spectra. The convergence thresholds for the electronic and ionic steps are set to 10^{-8} eV and 0.1 meV/Å respectively.

We treat the chemical 50/50 mixing of Pr and Ca in PCMO with a supercell approach, where either a Pr or Ca atoms occupy half of the A-sites positions within the 40 atoms unit cell. In total, we generated four unit cells with different distributions of Ca and Pr. Next, we compute for these four different configurations the total energies for different antiferromagnetic arrangements of the Mn spin moments. An A-type ordering (Fig. 2) is found as the lowest energy magnetic ordering. The real magnetic unit cell is bigger than the supercell considered here and thus cannot be used. This however has only little influence to the result, a different magnetic ordering only slightly changing the size of the gap. For this magnetic structure we then relax the atomic positions within the unit cell. We list the structural data of one exemplary unit cell after the force minimization in Table 2. During the structural relaxation, the symmetry of the crystal was constrained to the $P2_1/m$ space group, which corresponds to the symmetry of the charge ordered (CO) state [6]. Overall, our obtained structures exhibit a good agreement with the experimental data of Goff et al [6], also given in Table II.

Next, we compute the phonon frequencies at the zone center (q=(0,0,0)) for all four

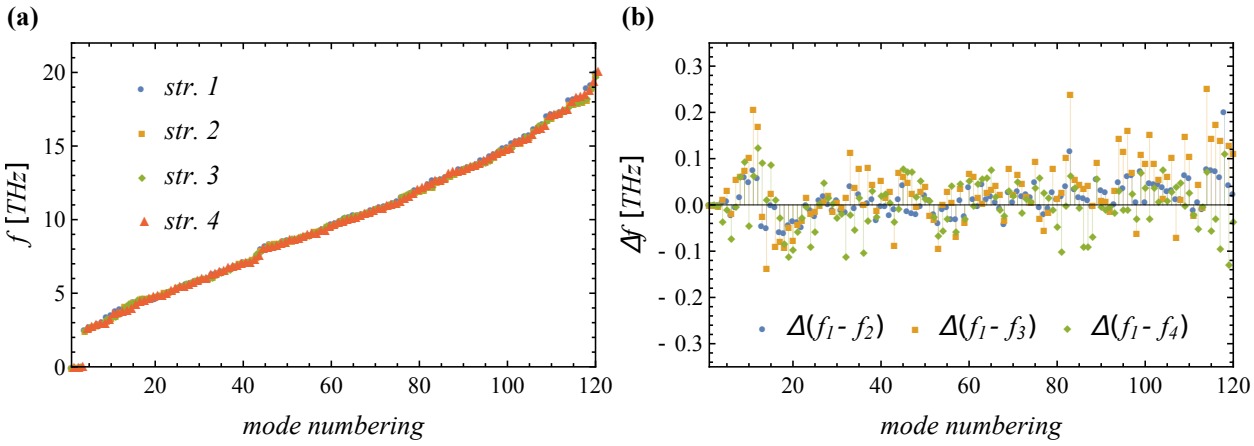

FIG. 3. Comparison of the phonon mode frequencies at q=(0,0,0) for four different distributions of Pr and Ca atoms within the PCMO structure. (a) Frequency as a function of mode numbering for all four structures and (b) the difference of phonon mode frequencies with respect to structure 1, which is given in Table II.

structures by calculating the force constant matrix using a finite difference approach as implemented in the Phonopy software package [7]. The 40 atoms unit cell exhibit 117 non-translational modes which are spanned by the irreducible representations of the 2/m point group. There are explicitly 31 A_g modes, 28 A_u modes, 35 B_u modes and 23 B_g modes. We note that the A_u and B_u modes exhibit a polarization along the c and a-b axis, respectively.

We show the computed phonon frequencies for the four distinct distributions of Pr and Ca atoms in Fig. 3 (a). All four structures exhibit very similar phonon frequencies. To quantify this observation, we computed further how the frequencies of the phonon modes changes between the four structures and show these differences in Fig. 3 (b). Each specific mode frequency does not vary more than 0.3 THz between the different structural configurations. Consequently, due to the insensitivity of the phononic system of PCMO on the Pr and Ca distribution, we concentrate in the following our discussion on one configuration with its structure given in Table II.

Lattice constants	a (DFT)	a (EXP)	b (DFT)	b (EXP)	c (DFT)	c (EXP)
	10.91 Å	10.87 Å	7.52 Å	7.49 Å	5.44 Å	5.43 Å
Atomic positions						
Atom	Wykoff position	x (DFT)	x (EXP)	y (DFT)	y (EXP)	z (DFT)	z (EXP)
Pr/Ca	e	-0.012	-0.014	0.250	0.250	0.002	0.008
Pr/Ca	e	-0.268	-0.266	0.250	0.250	0.485	0.490
Pr/Ca	e	0.477	0.485	0.250	0.250	0.011	0.009
Pr/Ca	e	0.232	0.238	0.250	0.250	0.499	0.491
Mn1	f	0.255	0.246	0.498	0.492	0.008	0.008
Mn2a	c	0.000	0.000	0.000	0.000	0.500	0.500
Mn2b	d	0.500	0.500	0.000	0.000	0.500	0.500
O1	e	0.001	0.008	0.250	0.250	-0.434	-0.436
O2	e	-0.239	-0.249	0.250	0.250	-0.078	-0.075
O3	e	-0.487	-0.492	0.250	0.250	-0.415	-0.422
O4	e	0.256	0.259	0.250	0.250	-0.074	-0.066
O5	f	0.355	0.360	0.460	0.461	0.299	0.293
O6	f	-0.110	-0.106	-0.464	-0.452	-0.224	-0.224
O7	f	-0.139	-0.144	0.464	0.469	0.263	0.262
O8	f	0.392	0.386	-0.455	-0.468	-0.212	-0.208

TABLE II. Comparison of experimental (EXP) [6] and calculated in this work (DFT) structural parameters of PCMO.

In the next step, we determine the mode displacement due to the excitation by a THz pulse. We thereby follow the approach of Juraschek et al. [8] and solve the dynamical equation for a harmonic oscillator driven by a pulsed excitation. The resulting displacement of the mode depends on both the mode specific dipole moment p^* and the matching of pulse bandwidth and mode frequencies. We show in Fig. 3 (a),(b) the mode polarities and the resulting displacements of polar modes due to the excitation with the THz pump pulse

provided during the experiment. The data shown are restricted to the A_u modes with the polarization along the c-axis corresponding to the experiment. Two modes exhibit a significant dipole moment (Fig. 4 (a)) and are found to be significantly excited by the THz pulse (Fig. 4 (b)). The main anharmonic displacements and changes in the electronic structure will be driven by the largest polar modes displacements. Consequently, we focus in the following on these two modes with frequencies 17.2 THz and 18.9 THz. The atomic displacement induced by the excitation of both modes is shown in Fig. 5 and the corresponding eigenvectors are given in Table III. Interestingly the stretching mode is excited only at the Mn^{3+} octahedra, while the Mn^{4+} ions are not moving. Each mode excites the stretching motion at a different Mn^{3+} sites (Mn2a or Mn2b from table II).

Ion	Mode 17 Thz	Mode 19 THz	Ion	Mode 17 THz	Mode 19 THz
Mn5	(-1.3, 1.0, 0)	(0, 0, -3.5)	O11	(0, 0, -1.4)	(0, 0, 0)
Mn6	(1.3, -1.0, 0)	(0, 0, -3.5)	O12	(0, 0, -1.4)	(0, 0, 0)
Mn7	(0, 0, -2.3)	(0, 0, 0)	O13	(3.8, -3.9, 0)	(0, 0, -1.4)
Mn8	(0, 0, -2.3)	(0, 0, 0)	O14	(3.8, -3.9, 0)	(0, 0, -1.4)
O1	(0,0,0)	(0, 0, 16.2)	O15	(-3.8, 3.9, 0)	(0, 0, -1.4)
O2	(0,0,0)	(0, 0, 16.2)	O16	(-3.8, 3.9, 0)	(0, 0, -1.4)
O3	(0, 0, -3.7)	(0, 0, 0)	O17	(0, 1.7, 0)	(0, 0, -1.1)
O4	(0, 0, -3.7)	(0, 0, 0)	O18	(0, 1.7, 0)	(0, 0, -1.1)
O5	(0, 0, 11.7)	(0, 0, 0)	O19	(0, -1.7, 0)	(0, 0, -1.1)
O6	(0, 0, 11.7)	(0, 0, 0)	O20	(0, -1.7, 0)	(0, 0, -1.1)
O7	(0, 0, 6.9)	(0, 0, 0)	O21	(1.3, -1.6, -1.4)	(0, 0, 0)
O8	(0, 0, 6.9)	(0, 0, 0)	O22	(1.3, -1.6, -1.4)	(0, 0, 0)
O9	(0, 0, -1.4)	(0, 0, 0)	O23	(-1.3, 1.6, -1.4)	(0, 0, 0)
O10	(0, 0, -1.4)	(0, 0, 0)	O24	(-1.3, 1.6, -1.4)	(0, 0, 0)

TABLE III. Eigenvectors in pm of each excited mode corresponding to a phonon amplitude $A = 1\sqrt{u}$Å. Ions that are not explicitely mentioned here do not move.

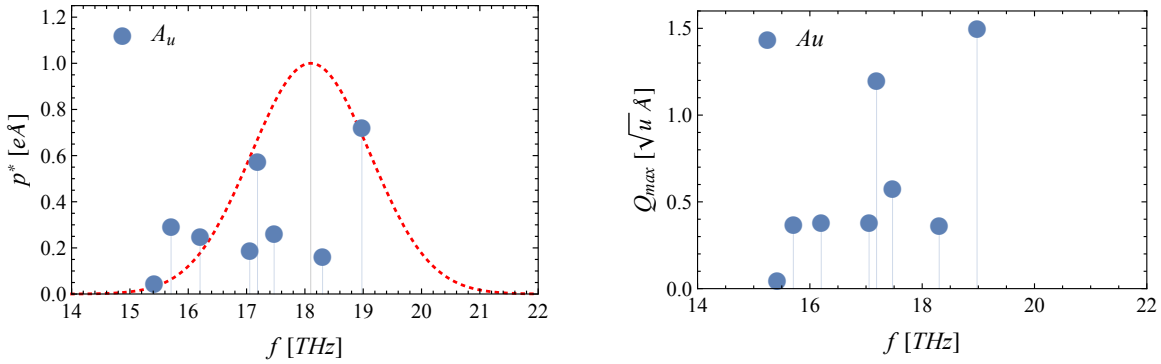

FIG. 4. (a) A_u mode polarity p^* in the range of the pulse frequency. The dashed red curve corresponds to the frequency width of the experimental pulse. (b) Resulting maximal mode displacement of polar A_u modes.

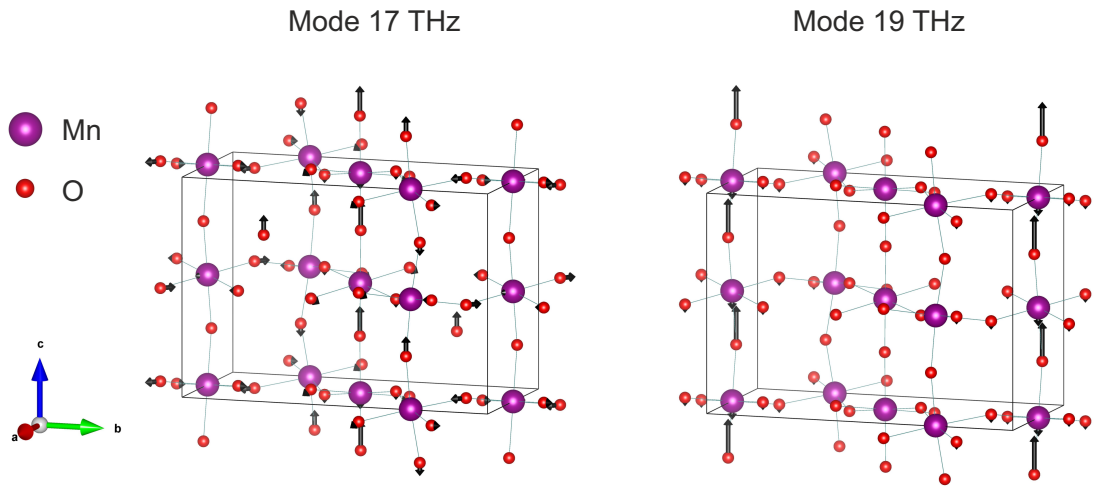

FIG. 5. Atomic displacement induced by the excitation of each modes at 17.2 THz and 18.9 THz (black arrows, scaled by a factor 7 for clarity). The main displacement is the stretching mode of the apical Mn-O bond along the c-axis shown in the inset of Fig. 1 (b) of the main text. The Ca and Pr ions do not move and are not displayed here for clarity.

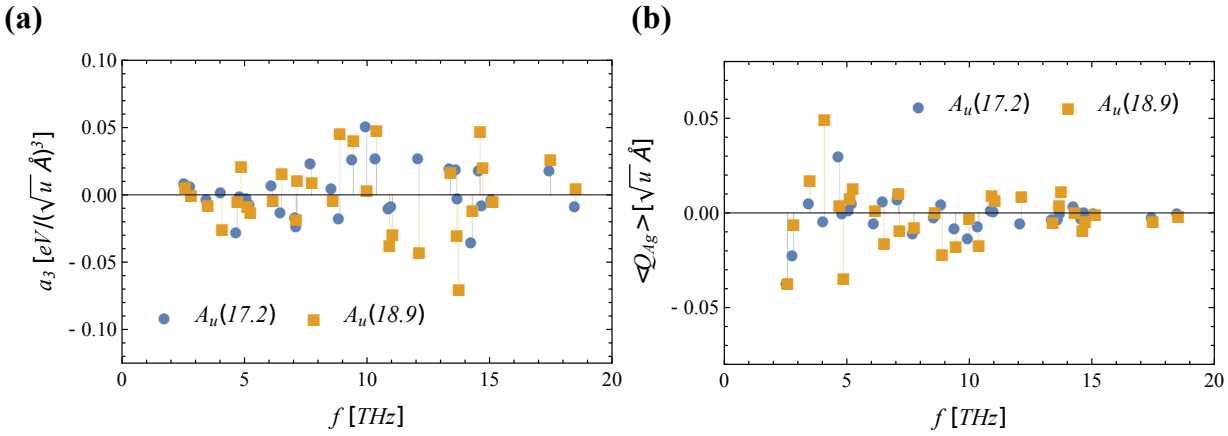

FIG. 6. (a) Cubic anharmonic coupling constants of the $A_u(17.2)$ and $A_u(19.9)$ polar modes with all other phonon modes of A_g symmetry. (b) Maximal amplitude of the A_g mode induced by the anharmonic coupling and displacement of the polar mode.

ANHARMONIC PHONON COUPLING

We also explore the anharmonic coupling of the two excited polar modes to other modes, comparable to the analysis by Subedi et al [9]. We restrict our analysis to the cubic coupling of potential given in the main text. Similar to Refs. [8, 10], we compute a_3 by performing frozen phonon calculations and fitting the resulting energy landscape to the potential given in the main text. We note that the cubic coupling is only allowed between the polar mode and modes of A_g symmetry. Consequently, we performed 62 separate calculations for each pair of polar and A_g mode.

Figure 6 (a) shows an overview of the obtained a_3 coupling constants over the entire frequency range. We note that the found cubic coupling constants are small compared to other materials as given in Refs [8–10]. Cubic anharmonicities between polar and A_g modes cause transient structural modulations by the A_g mode which are driven by the polar mode displacement [10]. The size of these modulations is given by

$$\langle Q_{\mathrm{A}_g} \rangle = \frac{a_3 Q_{\mathrm{IR}}^2}{\omega_{\mathrm{A}_g}^2}. \tag{1}$$

Thus beside the coupling constants, the excitation strength of the polar mode and the mode frequency of the A_g mode also influence the displacement of the A_g mode. To quantify the distortion created by the cubic anharmonicities we evaluate Eqn. 1 for our computed coupling constants in combination with the amplitudes of the polar mode created by the

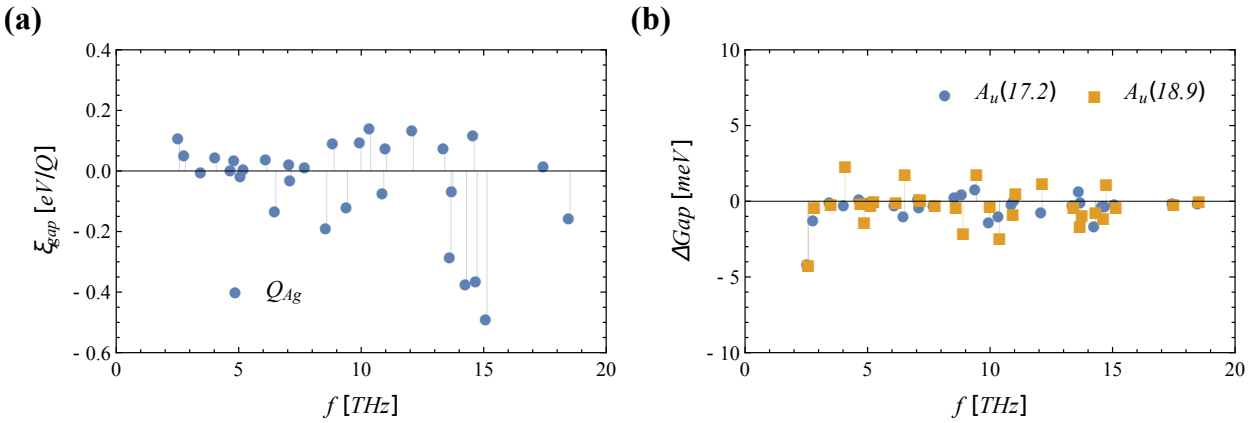

FIG. 7. Effects of the induced Raman displacement on the gap. (a) Linear coefficient of the mode amplitude dependent gap for all calculated Raman modes. (b) Gap change as a function of the induced Raman displacement by both excited modes.

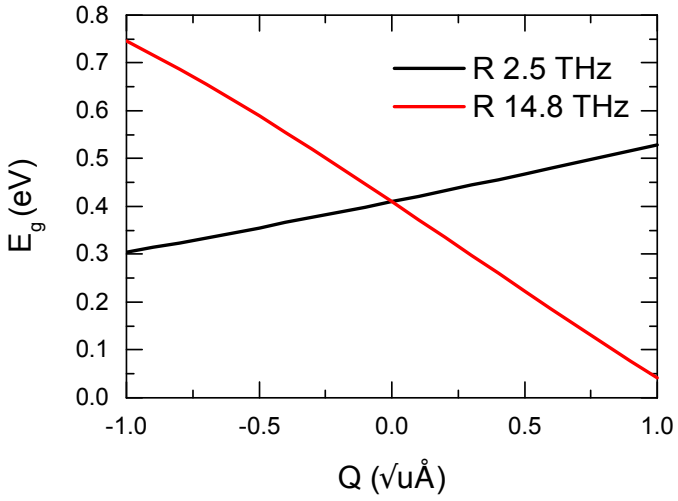

FIG. 8. Gap as a function of two Raman modes amplitude. A mostly linear dependence is observed, as expected from the mode symmetries.

largest fluences. Figure 6 (b) shows the resulting displacements of A_g modes created by both polar modes. Overall, we find that cubic anharmonicities only create negligible to small displacements of the A_g modes. Mode amplitudes of 0.05 $\sqrt{u}$/Åcorrespond to average atomic displacements of 0.02 pm, which are too small to exhibit a sizeable effect.

Although the induced distortions are very small, we checked the behavior of the gap as a function of the Raman modes amplitudes and their corresponding displacements. These

results are summarized in Fig. 7. Some modes indeed couple strongly to the gap (Fig. 7 (a)); however these are high frequency modes whose displacements are tiny, resulting in a negligible change of the gap energy (Fig. 7 (b)). In Figure 8, we show the gap as a function of the mode amplitude for two Raman phonons: a mode at 2.4 THz, which is displaced the most and a mode at 14.8 THz, which has a large effect on the gap. The gap depends linearly on the mode amplitude and the direction of the displacement leads to a reduction of the gap, as predicted by Subedi et al. in Ref. [9]. However, the overall contribution of the Raman modes is estimated to -15 meV, clearly too small to induce the transition to the metallic state.

* Corresponding author: vincent.esposito@psi.ch

[1] J. P. Perdew, K. Burke, and M. Ernzerhof, Physical review letters **77**, 3865 (1996).

[2] G. Kresse and J. Furthmüller, Physical review B **54**, 11169 (1996).

[3] P. E. Blöchl, Physical Review B **50**, 17953 (1994).

[4] V. I. Anisimov, F. Aryasetiawan, and A. Lichtenstein, Journal of Physics: Condensed Matter **9**, 767 (1997).

[5] Y. Okimoto, Y. Tomioka, Y. Onose, Y. Otsuka, and Y. Tokura, Phys. Rev. B **59**, 7401 (1999).

[6] R. J. Goff and J. P. Attfield, Phys. Rev. B **70**, 140404 (2004).

[7] A. Togo and I. Tanaka, Scripta Materialia **108**, 1 (2015).

[8] D. M. Juraschek, M. Fechner, and N. A. Spaldin, arXiv preprint arXiv:1607.01653 (2016).

[9] A. Subedi, A. Cavalleri, and A. Georges, Phys. Rev. B **89**, 220301 (2014).

[10] M. Fechner and N. A. Spaldin, Phys. Rev. B **94**, 134307 (2016).